On the mechanism and energetics of electrochemical alloy formation between mercury and platinum for mercury removal from aqueous

Electrochimica Acta 507 (2024) 145137

Contents lists available at ScienceDirect

Electrochimica Acta

journal homepage: www.journals.elsevier.com/electrochimica-acta

On the mechanism and energetics of electrochemical alloy formation between mercury and platinum for mercury removal from aqueous solutions

Vera Roth [a], Mikael Valter-Lithander [a], Linnéa Strandberg [a], M. Reza Bilesan [b], Julia Järlebark [a,c], Jan Jamroz [d,e], Björn Wickman [a,*]

[a] Department of Physics, Chemical Physics, Chalmers University of Technology, SE-41296 Gothenburg, Sweden
[b] Department of Separation Science, School of Engineering Science, LUT University, FI-53850 Lappeenranta, Finland
[c] Department of Chemistry and Chemical Engineering, Applied Chemistry SE-41296, Gothenburg, Sweden
[d] Department of Physics, Materials Physics, Chalmers University of Technology SE-41296, Gothenburg, Sweden
[e] Faculty of Physics, Warsaw University of Technology, PL-00662, Warsaw, Poland

ARTICLE INFO

Keywords:
Mercury removal
Platinum
Electrochemical alloy
EQCM
DFT

ABSTRACT

Mercury pollution is an acute global concern threatening the health of humans and wildlife. Thus, there is a need for new and improved techniques to reduce emissions and remove toxic mercury from aqueous environments. Electrochemical alloy formation, specifically between mercury ions in aqueous solution and a platinum electrode, emerges as a promising solution. Through analysis of reaction mechanisms and energetics related to the formation and dissolution of the $PtHg_4$ alloy, this study aims to deepen our understanding of the underlying processes of effective electrochemical mercury removal. Potentiodynamic measurements indicate rapid alloy formation at a clean platinum surface, proceeding with only trace amounts of metallic mercury on the surface. However, once the electrode surface has sufficient mercury coverage with an alloy thickness of around 1.5 nm, clear evidence of metallic mercury on the surface is observed. Furthermore, the amount of absorbed mercury on the cathode increases linearly in time. The onset potential for the alloy formation is experimentally determined using electrochemical quartz crystal microbalance with dissipation monitoring to be approximately 0.64 V vs. SHE, and the alloy dissolution (oxidation) onset potential is found to be approximately 0.98 V vs. SHE, at a mercury ion concentration of 10 mg/L. Density functional theory calculations are used to provide a theoretical value for the reversible potential from a thermodynamics perspective, yielding a value of 0.78 V vs. SHE at a mercury ion concentration of 10 mg/L. This value is in excellent agreement with the experimental results, suggesting an overpotential of about 0.14 and 0.20 V for the alloy formation and oxidation, respectively. These findings provide important information on the reaction mechanisms and overpotentials of the $PtHg_4$ alloy formation and dissolution, which are key factors for development of large-scale mercury removal based on this technique, as well as fundamental understanding of the electrochemical alloy formation between mercury ions and platinum.

1. Introduction

Mercury (Hg) pollution is a serious global concern due to the high toxicity, potential for bioaccumulation, and pervasive mobility through ecosystems, posing risks to environmental health and human safety [1, 2]. Although Hg can occur naturally in the environment, human activities such as coal combustion, mining, and waste disposal significantly contribute to the elevation of Hg levels both at a local and a global scale. Through human activities, it is estimated that 1.5 million tonnes of Hg were released between the years 1850 and 2010, and current annual emissions are estimated to be around 2000 tonnes [3]. Once Hg is emitted, it continues to persist and cycle in the environment for centuries, or even millennia, before eventually settling in deep ocean sediments or subsurface soils [4]. Water plays a critical role in the mobility and spread of Hg, accounting for about 60 % of Hg's environmental cycling [5]. As a result, addressing Hg contamination in water is

* Corresponding author.
E-mail address: bjorn.wickman@chalmers.se (B. Wickman).

https://doi.org/10.1016/j.electacta.2024.145137
Received 25 June 2024; Received in revised form 6 September 2024; Accepted 22 September 2024
Available online 23 September 2024

essential to curb its extensive spread and protect all living beings from its harmful effects.

Different techniques have been developed for Hg removal from aqueous solutions, such as ion exchange, precipitation, solvent extraction, and membrane filtration [6]. Despite their availability, current methods have several limitations and challenges, e.g., low selectivity for Hg and insufficient removal rates. Certain methods are also highly sensitive to the pH of the solution, which can limit their effectiveness in removing Hg, as well as the management of secondary wastes and Hg-laden materials, which can be complex and expensive [6–10]. The toxic nature of Hg and the shortcomings of existing methods highlight the urgent need for more effective and efficient removal solutions.

We have recently introduced a method for Hg removal from aqueous solutions that aims to address some of the limitations of existing Hg removal techniques [11–14]. This method is based on the electrochemical alloy formation between Hg and a metal electrode, and is suitable for various applications, such as treating concentrated acids, industrial effluents, and natural waters. The selection of the electrode material is paramount in forming a stable Hg alloy. When platinum (Pt) is used as the cathode electrode material, Hg ions undergo electrochemical reduction and form an amalgam with Pt. Supporting this, X-ray diffraction (XRD) analysis of a saturated Pt on glass electrode indicated that $PtHg_4$ is the predominant phase formed [14].

While Pt is often preferred as electrode material, alternative materials like copper (Cu) and gold (Au) have also been considered. However, Cu exhibits instability in corrosive solutions, such as oxidizing acids, and can degrade in water without potential control. Furthermore, Cu will be oxidized and dissolved at the positive potentials required for Hg alloy oxidation, rendering Cu-based electrodes unsuitable for reuse and regeneration [13,15]. Although Au represents a stable alternative and could serve as a potential electrode material, it is currently more expensive than Pt [16], and in addition, the most stable Au-Hg alloy (Au_3Hg) has a significantly lower Hg binding capacity, holding 12 times less Hg per atom of noble metal than the $PtHg_4$ phase [17]. Using Pt as the electrode material for Hg removal via electrochemical alloy formation has been proven highly effective for decontaminating solutions in both environmental and industrial contexts [12]. The method exhibits a high selectivity for Hg, efficiently removing Hg ions even in the presence of various other cations such as calcium, cadmium, copper, iron, magnesium, manganese, sodium, nickel, lead, and zinc, as well as anions like chloride and nitrate [14]. Notably, the removal efficiency remains consistent across a pH range of 0 – 6.6 and is unaffected by corrosive acids [11,14]. In addition, the process is reversible, facilitating safe recovery of Hg and the subsequent regeneration of the Pt electrodes [14]. The energy requirements of the method are relatively low, for practical application, the power requirement is expected to be around 50 $\mu W/cm^2$ [14].

Past studies have extensively investigated several aspects of the Pt-Hg system [18–24], focusing on the solid-state interactions of metallic Hg at the Pt interface, and the characterization of the formed compounds. To further develop the electrochemical alloy formation as a Hg removal method, it is important to address other aspects and deepen our understanding of the complex reaction mechanisms at play under electrochemical conditions from metallic Pt and Hg ions. One critical aspect that has not yet been determined is the reversible potential of the electrochemical alloy formation. Identifying this potential, along with the practical overpotentials for both the formation and dissolution of the $PtHg_4$ alloy, is key in the further development for practical applications. In addition, there are outstanding questions regarding the formation of specific intermediates, during the alloy formation process, particularly concerning the formation of metallic Hg on the electrode surface. These intermediates are important as they may significantly influence the overall Hg removal efficiency and the subsequent formation of the $PtHg_4$ alloy.

In this work, cyclic voltammetry (CV) is conducted with preceding potential holds to adsorb varying amounts of Hg on the electrode. The absorbed Hg is subsequently stripped during the CV scans to monitor different forms of Hg on the electrodes, as alloy or metallic Hg as well as the possibility to oxidize absorbed Hg. Further experiments, using electrochemical quartz crystal microbalance with dissipation monitoring (EQCM-D), identify the onset potentials for both the formation and dissolution of the alloy. In addition, the dissipation monitoring in EQCM-D offers insights into the validity of the Sauerbrey equation and the viscoelastic properties of the film forming on the surface, including the effects of surface roughness. These aspects are generally not captured by standard EQCM, thus using EQCM-D can enable deeper understanding of the alloy properties and formation processes. A comparison between experimental findings on onset potentials with Density Functional Theory (DFT) calculations reveal a significant concordance, demonstrating strong agreement between the experimental results and theoretical predictions.

2. Methods

2.1. Working electrode fabrication

For EQCM-D experiments, AT-cut quartz crystal sensors (ø14 × 0.5 mm, resonant frequency 4.95 MHz ± 50 kHz, LAB Analytical) were used as the working electrode (WE). The sensors were coated with 200 nm of Pt with 3 nm of titanium (Ti) as an adhesion layer using physical vapor deposition (base pressure ~10^{-7} mbar, Lesker PVD 225), where a Pt circle pattern was made using a deposition mask with a diameter of 5 mm and a 1 mm connection strip. For CV measurements, polished fused silica glass (15 × 30 × 0.5 mm, Mark Optics Inc.) was used as substrates. The glass electrodes were coated with 100 nm of Pt and 10 nm of Ti using the same deposition system as for the quartz crystal sensors. Using a deposition mask, a pattern of Pt and Ti was coated on the electrode with 15 × 15 mm square at the bottom and a 1 mm connector strip to the top. Schematic illustrations of all WEs used can be seen in the **SI**.

2.2. Electrolyte preparation

For EQCM-D experiments, H_2SO_4 (97 %, Suprapur, Merck) was diluted to a concentration of 0.5 M with pure water (>18 MΩ·cm, Milli-Q EQ 7000) and an initial Hg^{2+} concentration of 10 mg/L using a Hg standard solution (1000 mg/L, TraceCERT, Merck). For CV, the acid was prepared in the same way as for the EQCM-D, both with and without addition of Hg.

2.3. Electrochemical measurements

CV was conducted using a three-electrode setup using 50 mL of 0.5 M sulphuric acid (H_2SO_4) as the electrolyte with initial Hg concentration of 10 mg/L. A Pt coated glass plate was used as the WE, a Pt wire as the counter electrode (CE), and mercury/mercurous sulphate (Hg/Hg_2SO_4) electrode (B3610+, SI Analytics) as the reference electrode (RE). CV was carried out at a scan rate of 50 mV/s on the WE in the electrolyte, both with and without Hg. Before recording each scan series, the potential was held at 0.18 V vs. SHE for durations ranging from 1 – 30 min to induce different amounts of alloy formation [12,14]. In addition, voltammograms were recorded also without any potential holding time (0 min), and in electrolyte with and without Hg. Notably even without a potential hold (0 min), Hg deposition occurs as the electrode is exposed to potentials below the Hg ion reduction potential during the scan.

EQCM-D experiments were similarly carried out using a three-electrode setup with a 0.5 M H_2SO_4 electrolyte solution with initial Hg concentration of 10 mg/L. A Pt surface of a quartz crystal sensor was used as the WE, with the aforementioned Pt wire and Hg/Hg_2SO_4 electrodes as the CE and RE, respectively. The resonance frequency changes of the crystal sensor for 3 different harmonics (3rd, 5th, and 7th) were continuously recorded throughout all the experiments. To determine the onset potential for the formation of the $PtHg_4$ alloy, a

cathodic potential scan was performed from 0.80 – 0.18 V vs. SHE at a scan rate of 0.1 mV/s. The potential scan was applied from a high enough potential (0.80 V vs. SHE), where no alloy formation occurs, and scanned to a sufficiently reductive potential (0.18 V vs. SHE), where it is well known that the alloy forms, without reaching hydrogen evolution reaction (HER) [25]. For determination of the onset potential for the alloy dissolution (oxidation), the EQCM-D experiment proceeded by applying a constant potential of 0.80 V vs. SHE to remove metallic Hg formed on the surface during the alloy formation process. Following this removal, the potential was scanned anodically from 0.80 – 1.16 V vs. SHE at a scan rate of 0.05 mV/s. A potential scan, instead of discrete constant potential experiments, makes it possible to investigate the alloy formation and its dissolution (oxidation) across a range of potentials in a single experiment. We argue that at these slow scan rates the system can be approximated as steady state in potential. Experiments at even slower scan rate (0.025 mV/s) gave the same results for onset potentials. All experiments were performed at a controlled temperature of 20 °C and with active stirring. Detailed illustrations of the experimental setups for both CV and EQCM-D are available in the **SI**.

During the EQCM-D experiments, the observed frequency shifts were recorded and correlated to the mass change on the quartz crystal sensor using the Sauerbrey equation [26]:

$$\Delta f = -\frac{2f_0 n}{A_s\sqrt{\rho_q \mu_q}}\Delta m \quad (1)$$

where the basic resonant frequency of the crystal sensor prior to any mass change is denoted by f_0, the number of overtone (3, 5, 7) is denoted with n, A_s is the active area, ρ_q is the density of quartz (2.648 g/cm^3), and μ_q is the shear modulus of quartz ($2.947\cdot10^{11}$ g/cm s^2) [27]. It can be noted that the Sauerbrey equation is only valid for determining the mass change under the condition that the film formed on the surface of the crystal sensor is rigid and thin, and where the energy losses are constant. In addition, the mass variation of the film should be relatively small when compared to the quartz crystal's initial mass, and uniformly distributed over the surface [28].

2.4. Density functional theory calculations

Density functional theory (DFT) calculations were performed using VASP [29–31] with the optB86b-vdW exchange-correlation potential [32,33]. The projector augmented wave method [34] was used to model the interaction between the valence electrons and the core. The Kohn-Sham orbitals were represented using a plane-wave basis set with a 450 eV cutoff energy, and a Gaussian smearing of 0.05 eV was applied to the Fermi-level discontinuity. The Brillouin zone was sampled with at least 8.2 k-points/Å in a Monkhorst-Pack grid [35].

Formation energies of $PtHg_x$ from solid Pt and Hg were calculated, to which a correction of 0.007 eV per Hg atom was added for the free energy difference in solid and liquid Hg [36]. We used this energy as an approximation for the free energy for the reactions, because: *i*) heat capacity and density differences are generally small for solids, meaning that enthalpy can be approximated as the formation energy [37], *ii*) the $T\Delta S$ term is small as the reactions are carried out at room temperature, and *iii*) the impact on the relevant reversible potentials is limited.

3. Results and discussion

3.1. Cyclic voltammetry study of $PtHg_4$ alloy formation and alloy oxidation

The electrochemical events occurring at a Pt surface, concerning the formation and subsequent oxidation of the $PtHg_4$ alloy, were studied through CV. Initially, CV was conducted at a scan rate of 50 mV/s in a 0.5 M H_2SO_4 electrolyte, both in the absence and presence of 10 mg/L Hg, to establish baseline voltammograms. Additional CV curves were then recorded following a potential hold at 0.18 V vs. SHE for durations ranging from 1 – 30 min. The subsequent cycling after each potential hold could effectively oxidize the alloy and regenerate the electrode, however, the number of cycles needed to restore the voltammogram to its baseline varied depending on the length of the initial potential hold.

Fig. 1**a** (0 min - 0 mg Hg/L) shows a stable cyclic voltammogram for a Pt glass WE without Hg, showcasing all the characteristic features typical of a Pt CV [38], including H^+ adsorption and desorption peaks, OH adsorption and an oxidation of Pt at higher potentials, as well as Pt oxide reduction. The electrochemical surface area (ECSA) was determined from the peaks associated with H^+ adsorption, using the charge between 0.04 – 0.42 V vs. SHE, and found to be 3.36 cm^2, assuming the surface charge of one monolayer of hydrogen on polycrystalline Pt is 210 μC/cm^2, and a surface coverage of 77 % [39]. The roughness factor (ECSA per projected surface area) was calculated to be 1.5 (where the projected surface area is 2.25 cm^2).

Fig. 1**b** (0 min - 10 mg Hg/L) shows the CV in the presence of Hg, where H^+ adsorption/desorption peaks are largely suppressed due to Hg ion reduction on the surface and formation of a Pt-Hg surface alloy [40]. It is also clear that the oxidation peak is shifted to higher potentials and becomes much larger than in the absence of Hg ions. This is due to the fact the new oxidation peak is a combination of Hg oxidation/dissolution and Pt surface oxidation. In Fig. 1**c–i** (1 – 30 min - 10 mg Hg/L), the oxidation peak is consistently observed at approximately 1.2 V vs. SHE across all voltammograms, regardless of hold duration. This peak, which grows over time, is attributed to the oxidation of $PtHg_4$ alloy, as detailed in previous work [12,14]. In Fig. 1**d–i** (3 – 30 min - 10 mg Hg/L), alongside the $PtHg_4$ alloy oxidation peak, another peak, between 0.6 – 0.7 V vs. SHE is becoming more pronounced and is attributed to metallic Hg forming on the electrode surface. The metallic Hg is removed from the surface during the first anodic scan after each hold, whereas the oxidation of the $PtHg_4$ alloy requires multiple cycles to complete. This is explained by the fact that for longer holding times, the amount of alloy on the electrode corresponds to several layers, and as the alloy oxidation occurs at potentials where Pt oxidizes, not all alloy has time to oxidize. In the subsequent cycles, the Pt oxide is reduced during the cathodic scan and more of the alloy can oxidize/dissolve again in the next anodic scan. Thus, an increased number of cycles is needed for electrode regeneration when a thicker alloy film has been formed. For holding times of 10 – 30 min, significant differences are observed in the cathodic sweep after the Pt oxide reduction peak around 0.6 V vs. SHE. These differences become more pronounced as the holding period increases and can be attributed to a roughening of the electrode surface resulting from the relatively fast oxidation of the multi-layered alloy film.

With increasing holding time at 0.18 V vs. SHE, there is a corresponding increase in the total charge stripped from the electrode surface. This charge is related to Hg oxidation and was determined by integrating the current over time for the potential range indicative of the electrochemical reactions of both the metallic Hg and the $PtHg_4$ alloy (approximately 0.38 – 1.58 V vs. SHE). In addition, the current over time was integrated for the potential range of only metallic Hg (depending on the length of potential hold, it ranges from approximately 0.56 to 0.74 V vs. SHE). For each voltammogram at holding times from 1 – 30 min, the charge for each cycle was calculated, adjusted for the baseline voltammogram, and the values summed to obtain a collective measure of the Hg mass accumulated over time. This charge can be directly related to the mass of Hg per unit area of the electrode, assuming all stripping charge is related to Hg oxidation, and all Hg strips as Hg^{2+}[41]. Fig. 2 shows the relationship between the holding time at 0.18 V vs. SHE, and the accumulated mass of Hg on the electrode. The total mass of Hg accumulated varies from approximately 900 to 11,000 ng/cm^2, over holding times of 1 and 30 min, respectively. This corresponds to an alloy thickness ranging from about 0.8 – 9.3 nm, or equivalently the thickness of about 1.3 – 15-unit cells, considering a surface roughness of 1.5.

This amount of alloy formed is well below the theoretical saturation limit which is 760 nm if a 100 nm Pt film is fully converted to $PtHg_4$

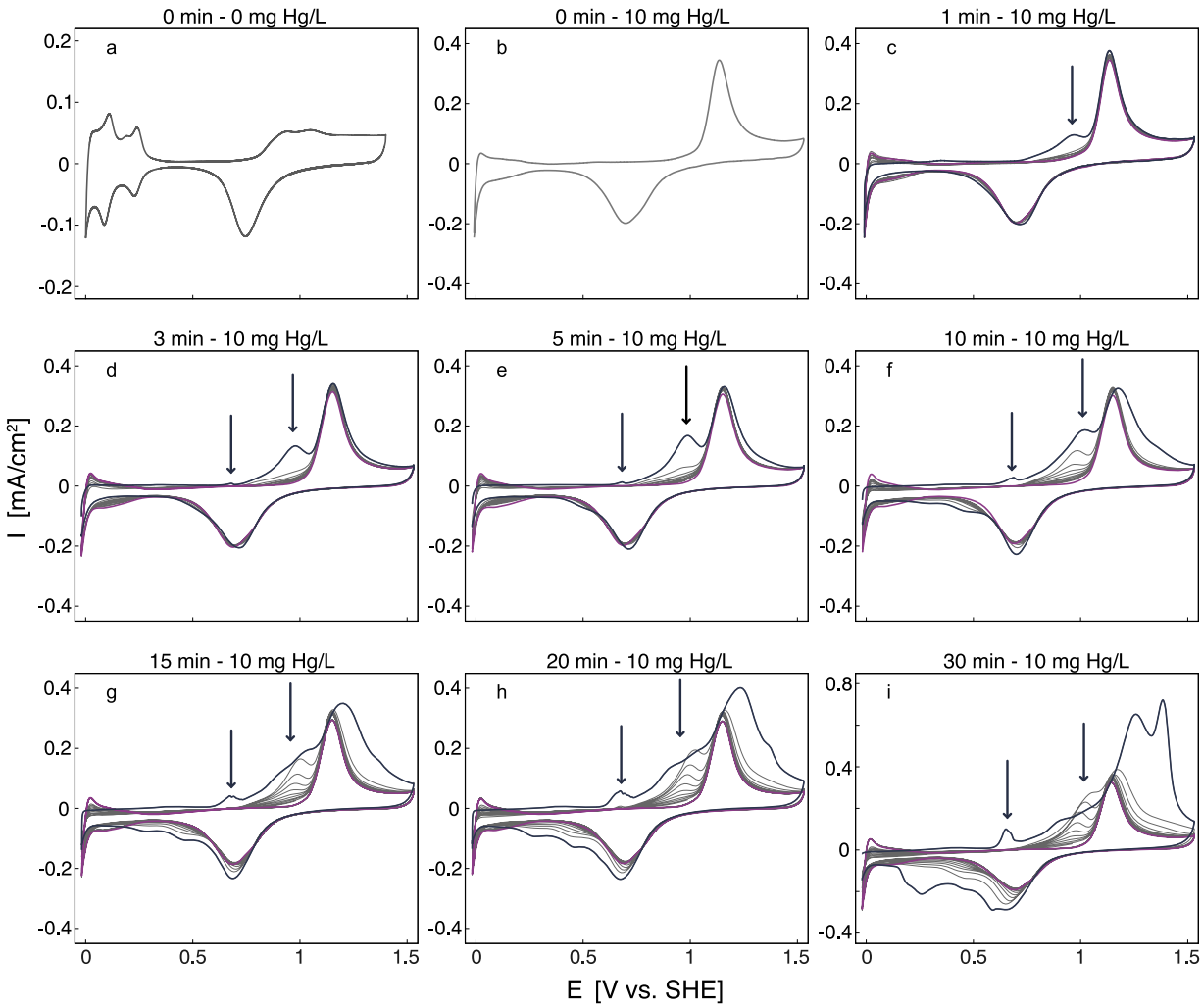

Fig. 1. Cyclic Voltammetry (CV) of Pt WE at 50 mV/s scan rate. For 0 min, 0 mg Hg/L (a), the electrolyte is 0.5 M H_2SO_4, while for the following 0 – 30 min (b – i), the electrolyte contains 10 mg/L of Hg. The potential was held at 0.18 V vs. SHE for 1 – 30 min (c – i), to induce $PtHg_4$ alloy formation, before performing subsequent CV scans. The dark blue trace indicates the initial CV cycle post potential hold, the grey trace depicts the following CV cycles, and the magenta trace marks the final CV cycle.

[14]. A clear linear relationship is depicted, indicating that the rate of Hg addition on the electrode remains constant over time, consistent with our previous findings [12]. Linear regression of the data provides an estimated rate of Hg uptake of approximately 20,000 ng/cm^{2}h for the total mass accumulated, and 400 ng/cm^{2}h for surface Hg, at a Hg ion concentration of 10 mg/L. The error bars represent an estimated uncertainty of around 5 %, primarily arising from the integration process, influenced by factors such as the choice of integration limits, the integration method, and the quality of the data.

3.2. *Onset potential of the $PtHg_4$ alloy formation and alloy oxidation*

EQCM-D was utilized to experimentally determine the onset potentials for both the formation and subsequent oxidation of the $PtHg_4$ alloy. Changes in resonance frequency and dissipation were recorded across three distinct harmonics (3rd, 5th, and 7th) of the crystal sensors, as shown in Fig. 3. The baseline fluctuations in frequency and dissipation observed using the EQCM-D were negligible, with changes of approximately $\pm$ 0.5 Hz and $\pm$ 1·10^{-7}, respectively, recorded over a 30-minute period. Additional details are provided in the **SI**.

Initially, applying a constant potential of 0.80 V vs. SHE results in no observable changes in the recorded frequency. After 10 min, a potential scan from 0.80 – 0.18 V vs. SHE at a scan rate of 0.1 mV/s results in a decrease in frequency, indicating mass uptake on the WE surface. The frequency initially decreases exponentially with potential until it begins to decrease linearly at around 35 min, and 0.60 V vs. SHE. This linear decrease continues until just before the 1-hour mark at 0.54 V vs. SHE, at which point divergence among the three harmonics is observed. The harmonics realign at around 1.6 h and 0.27 V vs. SHE and continue to decrease linearly until the end of the potential scan at 2 h and 0.18 V vs. SHE. Following the alloy formation, a constant potential of 0.80 vs. SHE is applied to strip the accumulated metallic Hg from the surface, supported by CV studies (Fig. 1) and previous literature, indicating that the $PtHg_4$ alloy oxidizes at a higher potential than metallic Hg [41]. After stripping the metallic Hg, a noticeable increase in frequency by approximately 100 Hz is observed. The frequency then stabilizes, indicating effective removal of metallic Hg from the electrode surface. Subsequently a potential scan from 0.80 – 1.16 V vs. SHE is performed. The frequency recorded exhibits only a slight increase until around 3 h, when the potential exceeds approximately 0.92 V vs. SHE, leading to an exponential increase in frequency (loss of mass). This increase can be attributed to the oxidation and dissolution of the $PtHg_4$ alloy. The exponential growth in frequency transitions to a more linear increase over time between approximately 1 – 1.1 V vs. SHE. In this region, oxidation does not depend on potential but proceeds at a constant rate in time. From 1.1 – 1.16 V vs. SHE, the rate changes, leading to a reduced

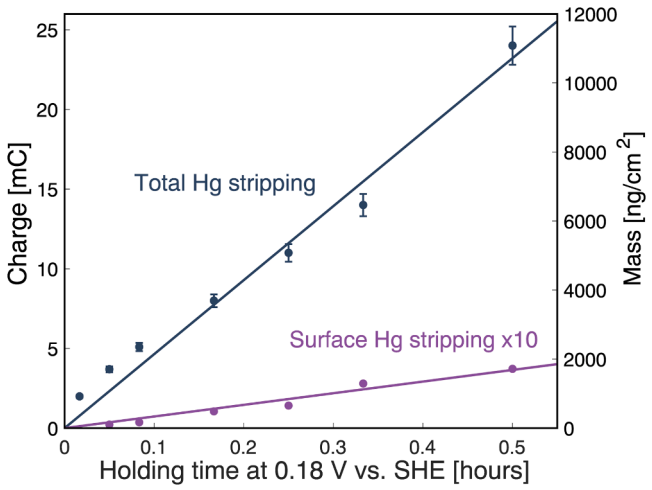

Fig. 2. Net positive charge associated with the stripping of Hg, from integrating the voltammograms in Fig. 1. The blue line represents the total net positive charge in the potential range of 0.38 – 1.58 V vs. SHE, and the magenta line represents the net positive charge in the potential range of approximately 0.56 – 0.74 V vs. SHE multiplied by 10 to make the data visible. Linear regression reveals a slope of approximately 20,000 ng/cm^2 h for the total Hg mass, and 400 ng/cm^{2}h for surface Hg.

slope and lower oxidation rate of the alloy.

Initially, when a constant potential of 0.80 V vs. SHE is applied, no changes in dissipation are observed, and dissipation changes remains relatively low throughout the alloy formation process. However, a sharp increase is observed during the divergence of the harmonics, peaking at approximately $3.5{\cdot}10^{-5}$ at around 1.38 h and 0.36 V vs. SHE. The dissipation change then quickly decreases and remain low as the resonance frequencies realign and stabilize towards the end of the potential scan for alloy formation. Following the stripping of the metallic Hg from the surface, a smaller but significant reduction in dissipation from about $2{\cdot}10^{-6}$ – $0.1{\cdot}10^{-6}$ is observed, further indicating its initial presence on the surface and effective removal. After this, the dissipation changes remain low, and minimal changes are observed throughout the oxidation of the alloy. The large increase in dissipation during the alloy formation, as well as the divergence of the three harmonics, suggest a change of the surface structure on the electrode. It is likely that the observed phenomenon is due to an increase in surface roughness, induced by the alloy formation, where more water is trapped on the rough surface and being dragged as the crystal oscillates. Initially, as the alloy forms on the surface, it appears as if it presents a smooth texture that transitions to a rougher state, thereby facilitating more water drag. However, as the alloy formation progresses, the surface transitions back to a smoother state [42]. CV of a quartz crystal, in a solution with and without 10 mg Hg/L, along with SEM analysis conducted prior to alloy formation and at the peak of the dissipation change, support the formation of a rougher surface. These findings are detailed in the **SI**.

The first increase in dissipation begins at a mass gain of approximately 2000 ng/cm^2 which corresponds to a mean alloy thickness of 1.7 nm on a smooth surface. However, it should be noted that the Pt surface on the crystals is not perfectly smooth, the ECSA is approximately 3.5 times larger than the projected area, meaning that the actual alloy thickness on the electrode surface is close to one layer when the notable increase in dissipation change occurs. Our interpretation is that the alloy film can form on the Pt surface and grow to about one layer without significantly changing the roughness of the surface. However, to further grow the alloy, it becomes necessary to pull out Pt atoms from beneath the alloy film, causing considerable surface roughening. This roughening continues until a mass gain of approximately 6500 ng/cm^2 (5.5 nm $PtHg_4$ on a flat surface) is reached, at which point the dissipation change levels off and then decreases again. At a mass gain of approximately 10,600 ng/cm^2 (10 nm $PtHg_4$ on a flat surface) the dissipation change returns to almost the same level as during the initial stage of alloy formation. This behaviour can be explained by the fact that once a sufficiently thick alloy film is formed, it has enough room to relax and lower its energy by forming a smoother film.

3.3. Determination of the onset potential of $PtHg_4$ alloy formation

Using the measured frequency changes obtained via EQCM-D, as shown in Fig. 3, and employing the Sauerbrey equation (Eq. (1)), we can calculate the mass of the $PtHg_4$ alloy formed on the crystal sensor. It can

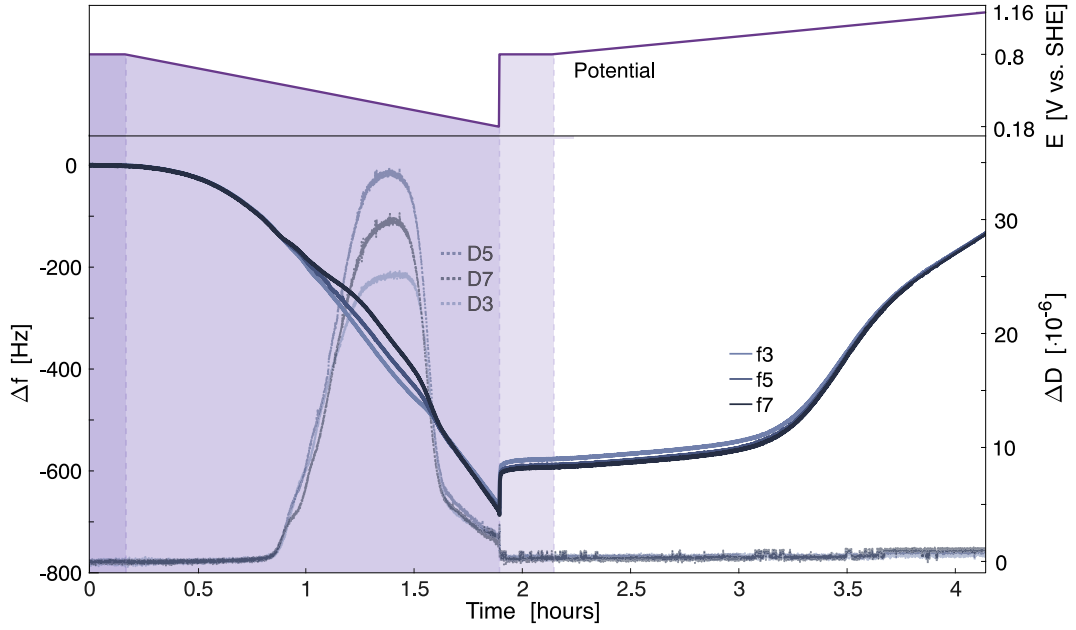

Fig. 3. EQCM-D recorded changes in frequency and dissipation across three harmonics (f3, f5, and f7) of a WE crystal sensor during $PtHg_4$ alloy formation scan from 0.80 – 0.18 V vs. SHE at 0.1 mV/s, followed by the removal of metallic Hg at 0.80 V vs. SHE, and an alloy oxidation potential scan from 0.80 – 1.16 V vs. SHE at 0.05 mV/s.

be assumed that in regions where the three harmonics overlap and dissipation change remains close to 0, the film is rigid, thereby justifying the application of the Sauerbrey equation for accurate mass calculation. A more comprehensive analysis of the relationship between recorded frequency, dissipation, and the application of the Sauerbrey equation, as well as Cu deposition from solution to confirm the accuracy of EQCM-D mass measurements, is detailed in the **SI**. It can also be noted that two deposition processes may occur simultaneously, $PtHg_4$ alloy formation and Hg plating. However, since Pt is already present on the WE, the observed mass increase is attributed solely to Hg deposition. As a results, we cannot accurately determine the ratio between these processes based merely on the frequency shift. Furthermore, the currents associated with Hg deposition are extremely low due to the low concentrations of Hg. The current measured during the deposition is dominated by the oxygen reduction reaction (ORR) from dissolved O_2 in the electrolyte.

Fig. 4 shows the mass increase during the alloy formation as a function of potential. The onset potential for the $PtHg_4$ alloy formation was determined using the tangent method [25], where linear extrapolation was made of data points where the three harmonics overlap, and dissipation change is close to 0. Therefore, linear extrapolation between 0.60 – 0.54 V and 0.27 – 0.18 V vs. SHE was made, with the x-axis intercept of zero mass change taken as the onset potential for $PtHg_4$ alloy formation, 0.64 V vs. SHE. More detailed discussion on the tangent method used is available in the **SI.**

Notably, the linear fit depicted in Fig. 4 present a slope of 25,000 ng/cm^{2}h, which closely aligns with the slope derived from the alloy formation process from the CV analysis in section 3.1. and shown in Fig. 2, which value is 20,000 ng/cm^{2}h. The discrepancy between the two slopes can be attributed to differences in the roughness of the Pt films used in CV and EQCM-D, as well as variations in other experimental conditions, such as continuous cycling vs. slow scanning.

3.4. Determination of onset potential of the $PtHg_4$ alloy oxidation

Similarly to the approach described in section 3.3, we can use the frequency changes measured through EQCM-D, as shown in Fig. 3, along with the Sauerbrey equation (Eq. (1)), to calculate the mass of $PtHg_4$ alloy on the crystal sensor. Fig. 5 shows the mass change as a function of potential during the potential scan ranging from 0.80 – 1.16 V vs. SHE. By using the tangent method once more and performing a linear

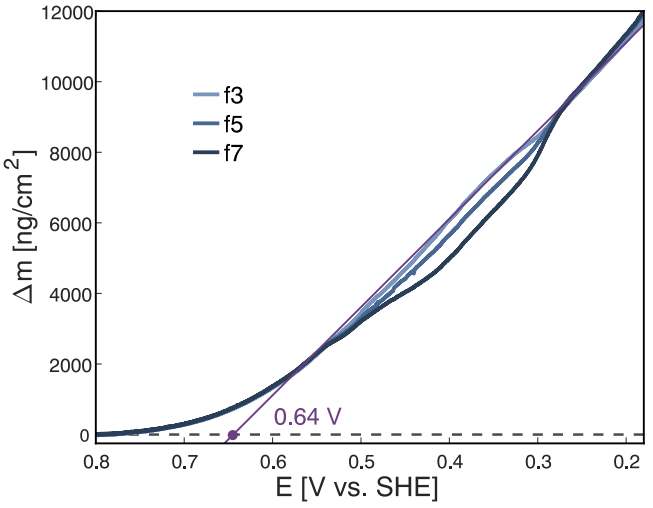

Fig. 4. Mass change as a function of potential during an alloy formationpotential scan from 0.80 – 0.18 V vs. SHE at 0.1 mV/s, for three different harmonics (f3, f5, and f7) of the WE crystal sensor. Linear extrapolations between 0.60 – 0.54 V and 0.27 – 0.18 V vs. SHE were made, where the intercept of zero mass change is taken as the onset potential for the alloy formation, 0.64 V vs. SHE.

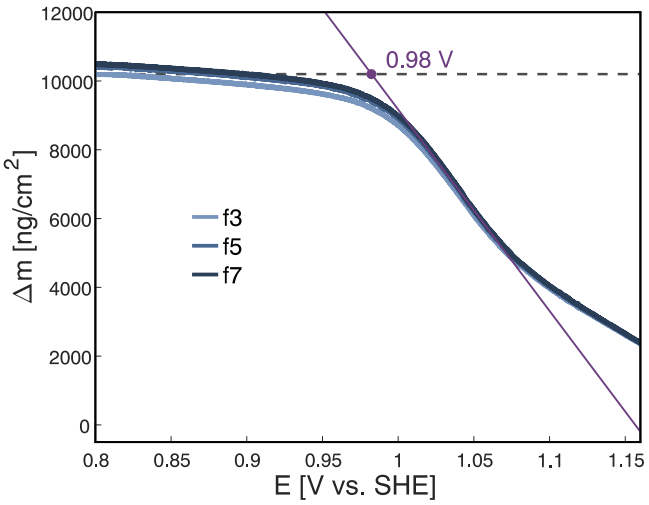

Fig. 5. Mass change as a function of potential, during an alloy oxidation potential scan from 0.80 – 1.16 V vs. SHE at 0.05 mV/s, for three different harmonics (f3, f5, and f7) of the WE crystal sensor. Using linear extrapolation between data set ranging from 1.02 – 1.07 V vs. SHE, onset potential of 0.98 V vs SHE was determined for the oxidation of the alloy.

extrapolation of the data set ranging from 1.02 – 1.07 V vs. SHE, the onset potential for the oxidation of the $PtHg_4$ alloy is determined to be 0.98 V vs. SHE.

3.4. Theoretical calculations of reversible electrode potentials for $PtHg_x$ alloys

Calculations were performed to generate a theoretical value for the standard electrode potential of $PtHg_4$ formation, for comparison with the experimental values obtained above. The calculations are based on nominal concentration of Hg and do not account for potential complexation with sulphate anions. Given the low mercury concentrations used in our experiments, it can be assumed that Hg_2SO_4 should be fully dissolved under these conditions [14,43].

Under a sweep from anodic potentials, $PtHg_4$ may be formed from divalent mercury ions (Hg^{2+}) or mercurous ions (Hg_2^{2+}):

$$Pt + 4Hg^{2+} + 8e^- \rightleftharpoons PtHg_4 \quad (2)$$

$$Pt + 2Hg_2^{2+} + 4e^- \rightleftharpoons PtHg_4 \quad (3)$$

These have the standard electrode potentials (E°, at 1 atm, 25 °C, 1 M and activity 1) [44].

$$Hg^{2+} + 2e^- \rightleftharpoons Hg_l,\ E^\circ = 0.853\ (\text{V vs. SHE}) \quad (4)$$

$$Hg_2^{2+} + 2e^- \rightleftharpoons 2Hg_l,\ E^\circ = 0.796\ (\text{V vs. SHE}) \quad (5)$$

Accounting for the experimental concentration with the Nernst equation, we get for the same Hg concentration as in the experiments (10 mg/L= 5.0·10^{-5} M Hg^{2+} or 2.5·10^{-5} Hg_2^{2+}):

$$\Delta E\left[Hg^{2+}, Hg\right] = \frac{0.059}{2}\log\left[Hg^{2+}\right] = -0.127\ \text{V} \quad (6)$$

$$\Delta E\left[Hg_2^{2+}, Hg\right] = \frac{0.059}{2}\log\left[Hg_2^{2+}\right] = -0.136\ \text{V}, \quad (7)$$

so that $E\left[Hg^{2+}, Hg\right] = 0.726$ V and $E\left[Hg^{2+}, Hg\right] = 0.660$ V vs. SHE. By setting the potential-dependent Gibbs free energy per Hg for these reactions equal,

$$2(0.726 - E) = 0.660 - E, \quad (8)$$

and solve for the potential, we get $E\left[Hg^{2+}, Hg_2^{2+}\right] = 0.793$ V vs. SHE for the equilibrium potential between the different Hg ions. Thus, >0.79 V vs. SHE, Hg^{2+} is most stable, <0.66 V vs. SHE metallic Hg is most stable, and Hg_2^{2+} is the most stable at potentials between these.

The Gibbs free energy per Hg for $PtHg_4$ formation (Eqs. (2)–(3)) can be written with the Hg equilibria as:

$$\Delta G(E) = \frac{1}{4}\Delta G\left[PtHg_4\right] - \frac{1}{4}\Delta G[Pt] - (\Delta G[Hg_l] + 2(0.726 - E))(eV) \quad (9)$$

$$\Delta G(E) = \frac{1}{4}\Delta G\left[PtHg_4\right] - \frac{1}{4}\Delta G[Pt] - (\Delta G[Hg_l] + (0.660 - E))(eV) \quad (10)$$

Setting the left-hand side of Eqs. (9)–(10) to zero and solving for the reversible potential, we get:

$$E\left[PtHg_4, Hg^{2+}\right] = 0.726 - \frac{1}{8}\Delta G_{PtHg_4}(\text{V vs. SHE}) \quad (11)$$

$$E\left[PtHg_4, Hg_2^{2+}\right] = 0.660 - \frac{1}{8}\Delta G_{PtHg_4}(\text{V vs. SHE}), \quad (12)$$

where $\Delta G_{PtHg_4} = \Delta G\left[PtHg_4\right] - \Delta G[Pt] - 4\Delta G\left[Hg_l\right]$ is the free formation energy. Using density functional theory, the free formation energy of $PtHg_4$ from solid Pt and Hg was found to be −0.39 eV, which gives:

$$E\left[PtHg_4, Hg^{2+}\right] = 0.775 \text{ V vs. SHE} \quad (13)$$

and

$$E\left[PtHg_4, Hg_2^{2+}\right] = 0.758 \text{ V vs. SHE} \quad (14)$$

The calculated value of ΔG_{PtHg_4} agrees well with −0.35 eV, reported by Robbins G. and Enke C. 1969 [24]. Guminski C. 1990, however, reported a more exergonic value −0.62 eV, in addition to −0.34 eV for $PtHg_2$ and −0.17 eV for PtHg [23]. By our calculations, we found $\Delta G_{PtHg_2} = -0.13$ eV and $\Delta G_{PtHg} = 0.00$ eV. The reason that the values from Guminski are circa 0.2 eV more favourable to alloy formation than ours is unclear to us. In Fig. 6, we show the free energy per Hg of all phases as a function of potential. From cathodic to anodic potentials, the most stable phase is $PtHg_4$, Hg_2^{2+}, and Hg^{2+}, with the equilibrium potentials from Eqs. (9)–(10) are marked.

The obtained values for the reversable potential of 0.76 V and 0.78 V vs. SHE agrees very well with the experimental observed $PtHg_4$ formation onset of 0.64 V vs. SHE, i.e., overpotentials of 0.12 V and 0.14 V, respectively, and the observed $PtHg_4$ oxidation onset of 0.98 V vs. SHE, i.e. an overpotential of 0.20 V and 0.22 V. This suggests that the overpotential is relatively symmetric (equally large) for the forward and backward reactions of $PtHg_4$ formation and oxidation, considering experimental errors and reference electrode potential accuracy.

4. Conclusion

The formation of the $PtHg_4$ alloy, from metallic Pt and Hg ions in solution is a non-spontaneous process. The determined onset potential of 0.64 V vs. SHE suggests that the process takes place close to the thermodynamic limit, which DFT calculations determine to be 0.76 V and 0.78 vs. SHE, at a Hg concentration of 10 mg/L in the form of Hg_2^{2+} and Hg^{2+}, respectively. The initial alloy formation proceeds without visible traces of metallic Hg; however, when the alloy coverage on the electrode surface is sufficiently high, the formation of metallic Hg on the surface is observed. The $PtHg_4$ alloy undergoes oxidation and subsequent dissolution with an onset potential of 0.98 V vs. SHE. Finding the onset of the alloy's dissolution is significant, as it enables the recovery of Hg from the Pt electrode for safe disposal and allows regeneration and reuse of the electrode. The regeneration process should be effective and time efficient. However, it is important to avoid excessively high potentials that could lead to unwanted side reactions and potentially damage the electrode material. It is critical to determine the onset potentials for the formation and dissolution of the $PtHg_4$ alloy, as this knowledge is essential for improving the Hg removal technique, ensuring its effectiveness, energy efficiency, and practical applicability.

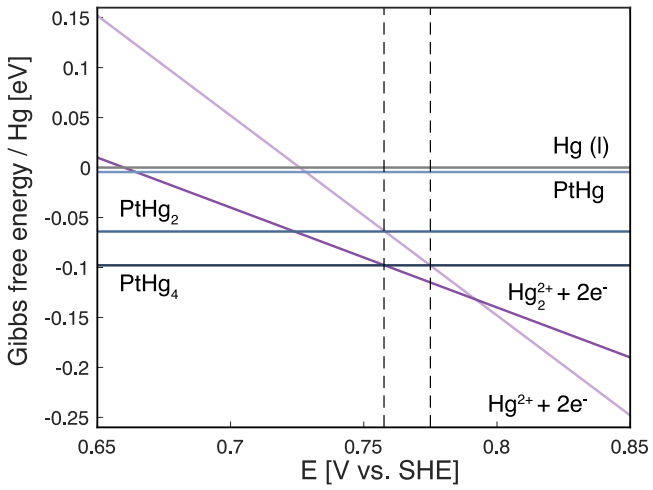

Fig. 6. Phase diagram for Hg at a concentration of 10 mg/L in the presence of metallic Pt. Phase transitions between Hg ions and $PtHg_4$ are marked with dashed vertical lines.

CRediT authorship contribution statement

Vera Roth: Writing – review & editing, Writing – original draft, Visualization, Investigation, Formal analysis, Data curation. **Mikael Valter-Lithander:** Writing – original draft, Visualization, Investigation, Formal analysis, Data curation. **Linnéa Strandberg:** Writing – original draft, Visualization, Investigation. **M. Reza Bilesan:** Writing – original draft, Investigation. **Julia Järlebark:** Writing – original draft, Visualization. **Jan Jamroz:** Investigation, Validation, Writing – review & editing. **Björn Wickman:** Writing – review & editing, Writing – original draft, Supervision, Resources, Project administration, Methodology, Funding acquisition, Conceptualization.

Declaration of competing interest

The authors declare the following financial interests/personal relationships which may be considered as potential competing interests: Björn Wickman reports financial support was provided by Swedish Research Council Formas. M. Reza Bilesan reports financial support was provided by European Regional Development Fund. Björn Wickman reports a relationship with Atium that includes: board membership. Björn Wickman has patent #EP 17,199,244.9 pending to Atium. If there are other authors, they declare that they have no known competing financial interests or personal relationships that could have appeared to influence the work reported in this paper.

Data availability

DFT data is available as a compressed file in the Supporting Information. Data from the electrochemical analysis is available upon request.

Acknowledgements

The authors gratefully thank for the financial support from the Swedish Research Council for Sustainable Development (Formas), project number 2019–01190, and the European Regional Development Fund (REACT-EU), Regional Council of Etelä-Karjala, project number A77605. We thank Gerard Montserrat Sisó for his contribution in PVD

deposition of platinum on the working electrodes.

Supplementary materials

Supporting information is available at the provided link, which includes additional experimental details, schematic illustrations of experimental setups and WEs, CV and SEM analysis of an EQCM-D quartz crystal, discussions on the EQCM-D baseline, the Sauerbrey equation, and the tangent method. A compressed file containing DFT data is also provided.

Supplementary material associated with this article can be found, in the online version, at doi:10.1016/j.electacta.2024.145137.

References

[1] L.T. Budnik, L. Casteleyn, Mercury pollution in modern times and its socio-medical consequences, Sci. Total Environ. 654 (2019) 720–734. https://doi.org/10.1016/j.scitotenv.2018.10.408.</bib.

[2] C.T. Driscoll, R.P. Mason, H.M. Chan, D.J. Jacob, N. Pirrone, Mercury as a global pollutant: sources, pathways, and effects, Environ. Sci. Technol. 47 (2013) 4967–4983. https://doi.org/10.1021/es305071v.</bib.

[3] D.G. Streets, H.M. Horowitz, D. Jacob, Z.F. Lu, L. Levin, A.F.H. ter Schure, E. M. Sunderland, Total mercury released to the environment by human activities, Environ. Sci. Technol. 51 (2017) 5969–5977. https://doi.org/10.1021/acs.est.7b00451.</bib.

[4] B. Gworek, W. Dmuchowski, A.H. Baczewska-Dąbrowska, Mercury in the terrestrial environment: a review, Environ. Sci. Eur. 32 (2020) 128. https://doi.org/10.1186/s12302-020-00401-x.</bib.

[5] P.A. Ariya, M. Amyot, A. Dastoor, D. Deeds, A. Feinberg, G. Kos, A. Poulain, A. Ryjkov, K. Semeniuk, M. Subir, K. Toyota, Mercury physicochemical and biogeochemical transformation in the atmosphere and at atmospheric interfaces: a review and future directions, Chem. Rev. 115 (2015) 3760–3802. https://doi.org/10.1021/cr500667e.</bib.

[6] K. Hua, X. Xu, Z. Luo, D. Fang, R. Bao, J. Yi, Effective Removal of mercury ions in aqueous solutions: a review, Curr. Nanosci. 16 (2020) 363–375. https://doi.org/10.2174/1573413715666190112110659.</bib.

[7] J.G. Yu, B.Y. Yue, X.W. Wu, Q. Liu, F.P. Jiao, X.Y. Jiang, X.Q. Chen, Removal of mercury by adsorption: a review, Environ. Sci. Pollut. Res. 23 (2016) 5056–5076, https://doi.org/10.1007/s11356-015-5880-x.

[8] Q. Wu, S. Wang, M. Hui, F. Wang, L. Zhang, L. Duan, Y. Luo, New insight into atmospheric mercury emissions from zinc smelters using mass flow analysis, Environ. Sci. Technol. 49 (2015) 3532–3539, https://doi.org/10.1021/es505723a.

[9] G. Crini, E. Lichtfouse, Advantages and disadvantages of techniques used for wastewater treatment, Environ. Chem. Lett. 17 (2019) 145–155, https://doi.org/10.1007/s10311-018-0785-9.

[10] J. Patterson, E. Barth, L. Stein, Aqueous mercury treatment, 1997.

[11] V. Roth, J. Järlebark, A. Ahrnens, J. Nyberg, J. Salminen, T.R. Vollmer, B. Wickman, Mercury removal from concentrated sulfuric acid by electrochemical alloy formation on platinum, ACS. ES. T. Eng. (2023), https://doi.org/10.1021/acsestengg.2c00417.

[12] E. Feldt, J. Järlebark, V. Roth, R. Svensson, P.K.G. Gustafsson, N. Molander, C. Tunsu, B. Wickman, Temperature and concentration dependence of the electrochemical PtHg4 alloy formation for mercury decontamination, Sep. Purif. Technol. 319 (2023) 124033, https://doi.org/10.1016/j.seppur.2023.124033.

[13] M.K.O. Bengtsson, C. Tunsu, B. Wickman, Decontamination of mercury-containing aqueous streams by electrochemical alloy formation on copper, Ind. Eng. Chem. Res. 58 (2019) 9166–9172, https://doi.org/10.1021/acs.iecr.9b01513.

[14] C. Tunsu, B. Wickman, Effective removal of mercury from aqueous streams via electrochemical alloy formation on platinum, Nat. Commun. 9 (2018), https://doi.org/10.1038/s41467-018-07300-z.

[15] B. Beverskog, I. Puigdomenech, Revised pourbaix diagrams for copper at 25 to 300°C, J. Electrochem. Soc. 144 (1997) 3476–3483, https://doi.org/10.1149/1.1838036.

[16] Live precious metal prices, metals Daily (n.d.). https://www.metalsdaily.com/live-prices/(accessed February 10, 2024).

[17] H. Okamoto, T.B. Massalski, The Au-Hg (Gold-Mercury) system, Bull. Alloy Phase Diagram. 10 (1989) 50–58, https://doi.org/10.1007/BF02882176.

[18] S.K. Lahiri, D. Gupta, A kinetic study of platinum-mercury contact reaction, J. Appl. Phys. 51 (1980) 5555–5560, https://doi.org/10.1063/1.327440.

[19] M.Z. Hassan, D.F. Untereker, S. Bruckenstein, Ring-disk study of thin mercury films on platinum, J. Electroanal. Chem. Interfacial. Electrochem. 42 (1973) 161–181, https://doi.org/10.1016/S0022-0728(73)80390-0.

[20] A.M. Hartley, A.G. Hiebert, J.A. Cox, Preparation and properties of a platinum-based mercury-film electrode, J. Electroanal. Chem. Interfacial. Electrochem. 17 (1968) 81–86, https://doi.org/10.1016/S0022-0728(68)80032-4.

[21] F.L. Fertonani, A.V. Benedetti, M. Ionashiro, Contribution to the study of the reaction of mercury with platinum and a platinum-iridium alloy, Thermochim. Acta 265 (1995) 151–161, https://doi.org/10.1016/0040-6031(95)02417-Z.

[22] G.R. Souza, I.A. Pastre, A.V. Benedetti, C.A. Ribeiro, F.L. Fertonani, Solid state reactions in the platinum–mercury system, J. Therm. Anal. Calorim. 88 (2007) 127, https://doi.org/10.1007/s10973-006-8037-9.

[23] C. Guminski, The Hg-Pt (Mercury-Platinum) system, Bull. Alloy Phase Diagram. 11 (1990) 26–32, https://doi.org/10.1007/BF02841581.

[24] G.D. Robbins, C.G. Enke, Investigation of the compound formed at a platinum-mercury interface, J. Electroanal. Chem. Interfacial. Electrochem. 23 (1969) 343–349, https://doi.org/10.1016/S0022-0728(69)80229-9.

[25] C. Batchelor-McAuley, Defining the onset potential, Curr. Opin. Electrochem. 37 (2023) 101176, https://doi.org/10.1016/j.coelec.2022.101176.

[26] D.A. Buttry, M.D. Ward, Measurement of interfacial processes at electrode surfaces with the electrochemical quartz crystal microbalance, Chem. Rev. 92 (1992) 1355–1379, https://doi.org/10.1021/cr00014a006.

[27] G. Sauerbrey, Verwendung von Schwingquarzen zur Wägung dünner Schichten und zur Mikrowägung, Zeitschrift Für Physik 155 (1959) 206–222, https://doi.org/10.1007/BF01337937.

[28] Biolin Scientific, The Sauerbrey Equation, n.d.

[29] G. Kresse, J. Hafner, Ab initio molecular dynamics for liquid metals, Phys. Rev. B 47 (1993) 558–561, https://doi.org/10.1103/PhysRevB.47.558.

[30] G. Kresse, J. Furthmüller, Efficiency of ab-initio total energy calculations for metals and semiconductors using a plane-wave basis set, Comput. Mater. Sci. 6 (1996) 15–50, https://doi.org/10.1016/0927-0256(96)00008-0.

[31] G. Kresse, J. Furthmüller, Efficient iterative schemes for ab initio total-energy calculations using a plane-wave basis set, Phys. Rev. B 54 (1996) 11169–11186, https://doi.org/10.1103/PhysRevB.54.11169.

[32] J. Klimeš, D.R. Bowler, A. Michaelides, Chemical accuracy for the van der Waals density functional, J. Phys.: Condensed Matter 22 (2010) 022201, https://doi.org/10.1088/0953-8984/22/2/022201.

[33] J. Klimeš, D.R. Bowler, A. Michaelides, Van der Waals density functionals applied to solids, (2011). https://doi.org/10.1103/PhysRevB.83.195131.

[34] P.E. Blöchl, Projector augmented-wave method, Phys. Rev. B 50 (1994) 17953–17979, https://doi.org/10.1103/PhysRevB.50.17953.

[35] H.J. Monkhorst, J.D. Pack, Special points for Brillouin-zone integrations, Phys. Rev. B 13 (1976) 5188–5192, https://doi.org/10.1103/PhysRevB.13.5188.

[36] J.E. Callanan, K.M. McDermott, E.F. Westrum, Fusion of mercury a new certified standard for differential scanning calorimetry, J. Chem. Thermodyn. 22 (1990) 225–230, https://doi.org/10.1016/0021-9614(90)90192-S.

[37] A. Jain, G. Hautier, S.P. Ong, C.J. Moore, C.C. Fischer, K.A. Persson, G. Ceder, Formation enthalpies by mixing GGA and GGA + U calculations, Phys. Rev. B 84 (2011) 045115, https://doi.org/10.1103/PhysRevB.84.045115.

[38] C.H. Hamann, A. Hamnett, W. Vielstich, Electrochemistry, 2nd ed., WILEY-VCH, 2007.

[39] T. Biegler, D.A.J. Rand, R. Woods, Limiting oxygen coverage on platinized platinum - relevance to determination of real platinum area by hydrogen adsorption, J. Electroanal. Chem. 29 (1971), https://doi.org/10.1016/s0022-0728(71)80089-x, 269-.

[40] S. Siahrostami, A. Verdaguer-Casadevall, M. Karamad, D. Deiana, P. Malacrida, B. Wickman, M. Escudero-Escribano, E.A. Paoli, R. Frydendal, T.W. Hansen, I. Chorkendorff, I.E.L. Stephens, J. Rossmeisl, Enabling direct H2O2 production through rational electrocatalyst design, Nat. Mater. 12 (2013) 1137–1143, https://doi.org/10.1038/nmat3795.

[41] S. Siahrostami, A. Verdaguer-Casadevall, M. Karamad, D. Deiana, P. Malacrida, B. Wickman, M. Escudero-Escribano, E.A. Paoli, R. Frydendal, T.W. Hansen, I. Chorkendorff, I.E.L. Stephens, J. Rossmeisl, Enabling direct H2O2 production through rational electrocatalyst design, Nat. Mater. 12 (2013) 1137–1143, https://doi.org/10.1038/nmat3795.

[42] Biolin Scientific, The QCM-D Principle, (n.d.). https://www.biolinscientific.com/faq/the-qcm-d-principle (accessed April 15, 2024).

[43] C.S. Kim, J.J. Rytuba, G.E. Brown, EXAFS study of mercury(II) sorption to Fe- and Al-(hydr)oxides, J. Colloid. Interface Sci. 270 (2004) 9–20, https://doi.org/10.1016/j.jcis.2003.07.029.

[44] A.J. Bard, R. Parsons, J. Jordan, Standard Potentials in Aqueous Solution, Routledge, 2017, https://doi.org/10.1201/9780203738764.